International Journal of Mechanical Sciences 172 (2020) 105368

Contents lists available at ScienceDirect

International Journal of Mechanical Sciences

journal homepage: www.elsevier.com/locate/ijmecsci

Voltage-controlled quantum valley Hall effect in dielectric membrane-type acoustic metamaterials

Weijian Zhou[a], Yipin Su[b], Muhammad[a], Weiqiu Chen[c], C.W. Lim[a,*]

[a] Department of Architecture and Civil Engineering, City University of Hong Kong, Tat Chee Avenue, Kowloon Tong, Kowloon, Hong Kong SAR, PR China
[b] School of Mathematics, Statistics and Applied Mathematics, NUI Galway, University Road, Galway, Ireland
[c] Department of Engineering Mechanics, Zhejiang University, Yuquan Campus, Hangzhou 310027, PR China

ARTICLE INFO

Keywords:
Active control
Membrane-type metamaterial
Topologically protected interface mode
Valley Hall effect

ABSTRACT

The research interest on phononic crystals now takes a new turn towards the acoustic/elastic analogies of the quantum concepts, e.g., the quantum Hall, quantum spin Hall and quantum valley Hall effects. One hallmark of these fundamental physical phenomena is the existence of topological edge/interface modes that propagate through the system along a designed path, with high robustness against week disorders. However, the working frequency ranges of the proposed topological phononic systems are usually very narrow, which therefore pose a clear limitation in practical applications. Motivated by this difficulty, we design and study a membrane-type metamaterial with tunable topological properties. The plane wave expansion method is employed to analyze its dispersion relation. A theoretical method is further proposed to conveniently calculate the valley Chern number. The theoretical and numerical results show the existence of topologically protected interface mode in the system. Its frequency range can be changed over a wide range by applying an electrical voltage, while the localization behavior of the interface mode is independent of the controlling operation. Consequently, we have successfully shown that the working frequency range of the topological phononic systems so derived can be significantly 'broadened' and hence the practical application may be dramatically widened.

1. Introduction

In recent decades, phononic crystals (PCs) have attracted enormous attention from scientific community due to their extraordinary physical characteristics and properties such as band gap (BG) [1–6], negative density [7,8], negative refraction [9,10], cloaking [11], etc. The BG, defined as a frequency range within which wave propagation is forbidden, is one of the most important properties of the PCs [12]. Early studies focus on designing PCs with wide or tunable BGs [13–16]. But in recent years, the research interests on PCs switch to the acoustic/elastic analogies of quantum concepts such as quantum Hall effect (QHE) [17–19], quantum spin Hall effect (QSHE) [20–24] and quantum valley Hall effect (QVHE) [25–30].

Generally, there are two broad ways to generate these fundamental phenomena. The first way is to break the system time-reversal (TR) symmetry. This was initially used in electronic and condensed matter, in which an applied strong magnetic field is capable of breaking the TR symmetry such that the single-way propagating edge waves can be realized [31]. Recently, this method was extended to PC systems by employing such components that the contained angle momentums can break the TR symmetry. Gyroscopic lattice [19] and rotational flow [17] were proposed to design these particular components and the unidirectional waves propagating along the edges were observed in the systems. Another way is to break the spatial symmetry [24]. In this way, the geometric phase in an one-dimensional (1D) PC system was inversed and the topologically protected interface mode (TPIM) was observed [32,33]. Besides, the analogies of QSHE [34–37] and QVHE [38–41] in two-dimensional (2D) PC systems have also been reported. In these 2D PC systems, TPIMs located in the BG ranges of bulk waves are observed. They can propagate along an interface between topologically trivial and nontrivial regions. Different from the interfacial mode caused by defects [42–44], the TPIMs are robust to disorders.

However, the frequency ranges of these reported TPIMs are very narrow. Particularly, the TPIMs in 1D PC systems only work at single frequency points [32,33]. Recently, Zhou et al. [45] proposed an inovative method to form and actively control the topological performances in a 'homogeneous' piezoelectric rod system by employing periodic A-B-A type electric boundary conditions. In practical applications, the disturbances of environmental conditions, such as mechanical loading [46,47], temperature [48,49] and external electric [50]/magnetic [51] fields, may affect the properties of topological PC devices and consequently shift their working frequencies. In these situations, the de-

* Corresponding author.
E-mail address: bccwlim@cityu.edu.hk (C.W. Lim).

https://doi.org/10.1016/j.ijmecsci.2019.105368
Received 9 August 2019; Accepted 15 December 2019
Available online 18 December 2019

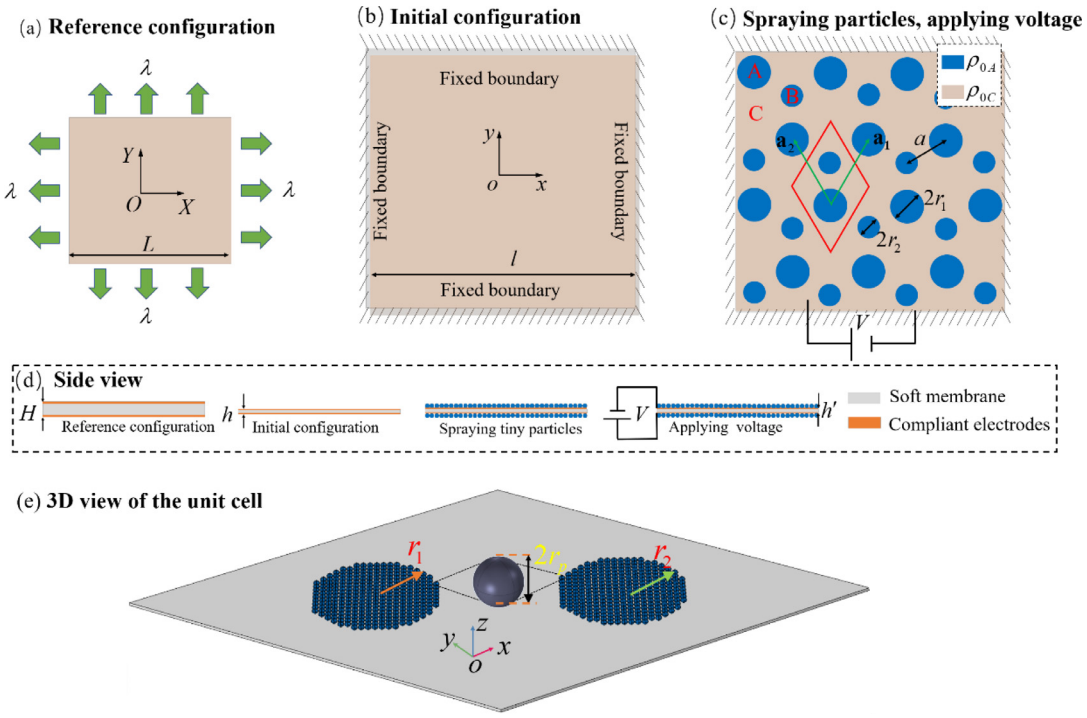

Fig. 1. Fabrication steps of soft MAM. (a) Reference state (undistorted state). (b) Initial (deformed) state. (c) Spraying fine particles and applying electrical voltage. Subdomains A and B are homogeneously bonded with tiny metallic particles. (d) Side view of the structure. (e) 3D view of the unit cell.

vices may lose their working efficacy. Thus, it is of great importance to broaden the frequency ranges of TPIMs. In addition, in intelligent technique applications, we may prefer the tunable devices with controllable properties. Motivated by these factors, in this paper we design and investigate an active membrane-type acoustic metamaterial (MAM) with controllable TPIM. Its frequency range can be changed over a wide range, so that its working frequency range can be significantly 'broadened'.

The soft MAM considered here is an extension of the soft MAM previously designed and reported [52]. It is fabricated by spraying tiny but heavy metallic particles onto a pre-stretched membrane, in a way that the sprayed regions form a hexagonal lattice. The membrane is sandwiched between two compliant electrodes of negligible thickness. An electrical voltage is then applied to the membrane to tune its tensile force. Here the low-frequency domain is of primary interest. Therefore, the MAM can be approximated as a density-heterogeneous membrane [52], and its dynamic performances can be described by the membrane model. The plane wave expansion (PWE) method [1] is applied to obtain the dispersion relation. A theoretical method is also established based on the PWE method to conveniently calculate the valley Chern number, an important invariant determining the QVHE in 2D PC systems. Numerical simulations show the existence of TPIM in the MAM system and its active control over a wide range can be realized. The theoretical and numerical simulations are beneficial and practical for the design and practical applications of tunable QVHE.

2. Theoretical modelling

The proposed soft density-heterogeneous MAM is illustrated in Fig. 1. A finite static deformation of a soft incompressible elastic membrane of thickness H and width L is first considered. In the undistorted reference configuration (Fig. 1a), the elastic membrane occupies a region B_r in the 3D Euclidean space. Its top and bottom surfaces are perfectively covered by compliant electrodes with negligible thickness. For a generic material particle at a position vector $\mathbf{X} = (X, Y, Z)$ within the domain of an undistorted membrane (reference configuration), this particle is deformed to a new position $\mathbf{x} = (x, y, z)$ via a smooth deformation $\mathbf{x} = \mathcal{U}(\mathbf{X})$ after finite deformation of the membrane to a new initial configuration (Fig. 1b). The deformation gradient of static deformation can be defined as $\mathbf{F} = \mathrm{Grad}\mathcal{U} = \partial\mathbf{x}/\partial\mathbf{X}$ and it is gven by $\mathbf{F} = \mathrm{diag}\{\lambda, \lambda, \lambda^{-2}\}$, where λ is the in-plane equibiaxial pre-stretch of the solid. The thickness and width of the deformed membrane now are $h = H\lambda^{-2}$ and $l = L\lambda$, respectively, where H and L are the undistorted thickness and width of membrane, respectively. Then, the horizontal boundaries of the membrane are fixed. After pre-stretching, tiny but heavy metallic particles are carefully sprayed onto its top and bottom surfaces, in a way that the regions with bonding particles (the blue region) are arrayed as a hexagonal lattice as shown in Fig. 1(c). The side view of MAM is shown in Fig. 1(d) and the 3D view of a unit cell after particle spraying is displayed in Fig. 1(e) for reference. The transfer printing technique [53] that was developed for fabricating flexible electronic devices, may be applied for bonding the metallic particles onto the membrane. In the initial configuration, the radii of subdomains A and B are r_1 and r_2, respectively, and the distance between two nearest bonded regions (or the lattice constant) is a. The radii r_1 and r_2 are set as $r_1 = r_0\xi$ and $r_2 = r_0(1-\xi)$, with r_0 being a defined reference radius and ξ being a structural parameter. The primary unit cell is marked by the red rhombic in Fig. 1(c), and the basis vectors of the periodic system are $\mathbf{a}_1 = (\sqrt{3}, 3)a/2$ and $\mathbf{a}_2 = (-\sqrt{3}, 3)a/2$. Then, the position of each unit cell can be expressed as $\mathbf{x}_C = m\mathbf{a}_1 + n\mathbf{a}_2$, with m and n being integers.

When bonding the particles onto the membrane, it is crucial to make sure that the particles are not in physical contact to each other. Thus, the interactions among tiny particles can be assumed to be very weak and will be neglected. Furthermore, the radius of each metal particle r_p is much smaller than the radii r_1 and r_2, such that the particles can be treated as lumped masses. The effects on the particle-bonding domains A and B can be considered in a homogenization sense in the low frequency range. In other words, we assume that the metallic particles do not change the thickness, but only contribute to the mass of membrane. Based on these assumptions, the in-plane stiffness and flexural stiffness of membrane remain homogeneous, but the mass density per unit area are periodically distributed. The density per unit area of subdomains A

and B is different from that of subdomain C, thus making the membrane density-heterogeneous. The mass density per unit area of subdomains A and B are approximated as $\rho_{0A}=\rho_{0B}\approx\frac{2}{3}\pi r_P\rho_P+h\rho_M$ and that of subdomain C is $\rho_{0B}=\rho_M h$, with ρ_P and ρ_M being the densities per unit volume of the particles and the membrane, respectively.

Next, we apply an electric voltage on the two compliant electrodes. Considering an incompressible membrane fixed on its horizonal boundaries, i.e. λ is fixed, the applied voltage will not induce any deformation but it only changes the tensile force N in the membrane. From the physical point of view, we have applied two external fields on the membrane in two steps, i.e. mechanical pre-stretching and then electrical voltage application. From a mathematical viewpoint, it is possible to assume that the two external fields are applied simultaneously [54] and consequently they can be analyzed based on the classical nonlinear electroelasticity theory [55,56], known as a two-configuration framework. For a membrane described by Gent model [57], the in-plane principal stress induced by the equi-biaxial pre-stretch λ and the applied electrical voltage V can be expressed as [58]

$$\sigma=\mu\frac{\lambda-\lambda^{-5}}{1-\left(2\lambda^2+\lambda^{-4}-3\right)/J_m}-\varepsilon\lambda^3E_0^2 \tag{1}$$

where μ and ε are respectively the membrane shear modulus and permittivity in the reference configuration, J_m is the dimensionless stiffening parameter and $E_0=V/H$.

3. Dispersion and topological performace

3.1. Governing equation and plane wave expansion method

An infinitesimal dynamic deformation $\mathbf{u}=\mathbf{u}(\mathbf{x},t)$ is superimposed on the static finite deformation $\mathbf{x}=\mathcal{U}(\mathbf{X})$. Here, we are only interested in the propagation of transverse wave, which are decoupled from the in-plane infinitesimal waves. We assume that the stretching force is large and the membrane is very thin. The classical membrane theory can be employed to approximately study the elastic transverse wave in the pre-stretched MAM. The equation of motion governing the time-harmonic transverse wave in the biaxially pre-stretched MAM is [52]

$$\rho_0(\mathbf{r})\omega^2u_3(\mathbf{r})+Nu_{3,11}(\mathbf{r})+Nu_{3,22}(\mathbf{r})=0 \tag{2}$$

where $\mathbf{r}$ is a position vectior, $N=\sigma\mathrm{h}$ is the principal in-plane tensile force per unit line, $\rho_0(\mathbf{r})$ is the density per unit area, ω is the angular frequency, $u_3(\mathbf{r})$ is the wave amplitude of the deflection w (i.e. $w=u_3(\mathbf{r})\mathrm{e}^{-\mathrm{i}\omega t}$ with $\mathrm{i}=\sqrt{-1}$) in the membrane, and a subscript following a comma denotes differentiation with respect to its argument.

The plane wave expansion method is applied to solve Eq. (2). Due to periodicity, the density function $\rho_0(\mathbf{r})$ can be expended as

$$\rho_0(\mathbf{r})=\sum_{\mathbf{g}}\rho_0(\mathbf{g})\mathrm{e}^{\mathrm{i}\mathbf{g}\cdot\mathbf{r}} \tag{3}$$

where $\mathbf{g}$ is the reciprocal-lattice vector in the initial configuration, expressed as $\mathbf{g}=m\mathbf{b}_1+n\mathbf{b}_2$, in which m and n are arbitrary integers, $\mathbf{b}_1$ and $\mathbf{b}_2$ are the basis vectors of the reciprocal lattice in the initial configuration. For the structure considered here, the basis vectors can be written as $\mathbf{b}_1=2\pi(\ \sqrt{3}\quad 1\ )^{\mathrm{T}}/(3a)$ and $\mathbf{b}_2=2\pi(\ -\sqrt{3}\quad 1\ )^{\mathrm{T}}/(3a)$. In this paper, the superscript 'T' denotes transpose operation.

The Fourier parameter $\rho_0(\mathbf{g})$ in Eq. (3) is generally determined by Fourier integration [52]. For the structure considered here they can be explicitly written as

$$\rho_0(\mathbf{g})=\begin{cases}f\rho_{0A}+(1-f)\rho_{0B} & (\mathbf{g}=\mathbf{0})\\ \left(\rho_{0A}-\rho_{0B}\right)F(\mathbf{g}) & (\mathbf{g}\neq\mathbf{0})\end{cases} \tag{4}$$

where $f=2\pi(r_1^2+r_2^2)/(3\sqrt{3}a^2)$ is the filling ratio, and $F(\mathbf{g})$ is a structural function given by

$$F(\mathbf{g})=2f_1\frac{J_1(|\mathbf{g}|r_1)}{|\mathbf{g}|r_1}\mathrm{e}^{-\mathrm{i}g_2a/2}+2f_2\frac{J_1(|\mathbf{g}|r_2)}{|\mathbf{g}|r_2}\mathrm{e}^{\mathrm{i}g_2a/2} \tag{5}$$

where $J_1(\bullet)$ is the first order Bessel function, $f_1=2\pi r_1^2/(3\sqrt{3}a^2)$ and $f_2=2\pi r_2^2/(3\sqrt{3}a^2)$.

According to the Bloch-Floquet theory, the solution to Eq. (2) can be expressed as

$$u_3(\mathbf{r})=\sum_{\mathbf{g}}U_3(\mathbf{g})\mathrm{e}^{\mathrm{i}(\mathbf{k}+\mathbf{g})\cdot\mathbf{r}} \tag{6}$$

where $\mathbf{k}=(\ k_1\quad k_2\ )^{\mathrm{T}}$ is the Bloch vector. By substituting Eqs. (3) and (6) into the Eq. (2), one obtains the governing equation

$$\omega^2\sum_{\mathbf{g}'}U_3(\mathbf{g}')\rho_0(\mathbf{g}-\mathbf{g}')-N\left[\left(k_1+g_1\right)^2+\left(k_2+g_2\right)^2\right]U_3(\mathbf{g})=0 \tag{7}$$

where $\mathbf{g}'$ is a reciprocal-lattice vector in the initial configuration.

3.2. The dispersion relation $\omega(\mathbf{k})$

To solve Eq. (7), we need to truncate the infinite summation in the Fourier expansions (3) and (6). For a selected m, $n=-T,\cdots,0,\cdots,T$, there are totally $(2T+1)^2$ plane waves involved in the analysis. Then, Eq. (7) can be reduced to a standard eigenequation as

$$\left(\mathbf{P}-\omega^2\mathbf{M}\right)\mathbf{U}_3=\mathbf{0} \tag{8}$$

where

$$\begin{aligned}&\mathbf{P}=\mathrm{diag}\left\{P_1\quad P_2\quad\cdots\quad P_{(2T+1)^2}\right\},\quad P_j=N\left[\left(\mathbf{k}+\mathbf{g}_j\right)_x^2+\left(\mathbf{k}+\mathbf{g}_j\right)_y^2\right]\\ &M_{ij}|_{i\neq j}=\left(\rho_{0A}-\rho_{0B}\right)F\left(\mathbf{g}_i-\mathbf{g}_j\right),\quad M_{ij}|_{i=j}=f\rho_{0A}+(1-f)\rho_{0B}\\ &\mathbf{U}_3=\left[\ U_3(\mathbf{g}_1)\quad U_3(\mathbf{g}_2)\quad\cdots\quad U_3\left(\mathbf{g}_{(2T+1)^2}\right)\ \right],\quad (i,j=1,2,\cdots,(2T+1)^2)\end{aligned} \tag{9}$$

For nontrivial solutions, the determinant of the coefficient matrix in Eq. (8) should vanish. Thus, the characteristic dispersion equation for the transverse waves in the MAM is

$$\left|\mathbf{P}-\omega^2\mathbf{M}\right|=0 \tag{10}$$

3.3. The calculation of valley Chern number

The valley Chern number is an important topological invariant to determine QVHE. When analyzing the size-dependent topological behaviors in PC beams at nanoscale, the PWE method is applied to theoretically calculate the Zak phase [32], which is used to analyze the topological properties in 1D system [33]. Here, this method is extended to the 2D PC system to theoretically calculate the valley Chern number.

From the eigenequation (8) and for a given Bloch vector $\mathbf{k}$, there are $(2T+1)^2$ values of positive ω as well as $(2T+1)^2$ normalized eigenvectors $\mathbf{U}_J(\mathbf{k})$. Then the periodic-in-cell part of the Jth eigenstate can be expressed as

$$\delta_{u_3}(J,\mathbf{k},\mathbf{r})=\mathrm{e}^{-\mathrm{i}\mathbf{k}\cdot\mathbf{r}}u_3(J,\mathbf{r})=\sum_{\mathbf{g}}U_J(\mathbf{k},\mathbf{g})\mathrm{e}^{\mathrm{i}\mathbf{g}\cdot\mathbf{r}} \tag{11}$$

Let us define the inner product of the Jth eigenstate as [19]

$$\left\langle\delta_{u_3}(J,\mathbf{k},\mathbf{r}),\delta_{u_3}\left(J,\mathbf{k}',\mathbf{r}\right)\right\rangle=\int_S\left[\delta_{u_3}(J,\mathbf{k},\mathbf{r})\right]^*\rho_0(\mathbf{r})\delta_{u_3}(J,\mathbf{k},\mathbf{r})\mathrm{d}S \tag{12}$$

where the superscript * denotes complex conjugation. By substituting the Fourier expansion of $\rho_0(\mathbf{r})$ as well as Eq. (11) into the inner product expression (12), one obtains

$$\begin{aligned}&\left\langle\delta_{u_3}(J,\mathbf{k},\mathbf{r}),\delta_{u_3}\left(J,\mathbf{k}',\mathbf{r}\right)\right\rangle\\ &=\int_S\sum_{\mathbf{g}}\sum_{\mathbf{g}'}\sum_{\mathbf{g}''}\left[U_J^*(\mathbf{k},\mathbf{g})\rho_0\left(\mathbf{g}'\right)U_J\left(\mathbf{k}',\mathbf{g}''\right)\right]\mathrm{e}^{\mathrm{i}(-\mathbf{g}+\mathbf{g}'+\mathbf{g}'')\cdot\mathbf{r}}\mathrm{d}S\end{aligned} \tag{13}$$

where $\mathbf{g}'$ and $\mathbf{g}''$ are reciprocal lattice vectors. Note that for $-\mathbf{g}+\mathbf{g}'+\mathbf{g}''\neq\mathbf{0}$, the integration in Eq. (13) is zero. Thus, Eq. (13) can be further simplified as

$$\left\langle\delta_{u_3}(J,\mathbf{k},\mathbf{r}),\delta_{u_3}\left(J,\mathbf{k}',\mathbf{r}\right)\right\rangle=S\sum_{\mathbf{g}}\sum_{\mathbf{g}'}U_J^*(\mathbf{k},\mathbf{g})\rho_0(\mathbf{g}-\mathbf{g}')U_J\left(\mathbf{k}',\mathbf{g}'\right) \tag{14}$$

Table 1
Material parameters.

Material	μ (MPa)	Relative permittivity	J_m	ρ_0 (kg/m^3)	Dielectric strength (MV/m)
Fluorosilicone 730 [60]	0.16767	7.11	6.28	1400	372
Tungsten	\	\	\	19,300	\

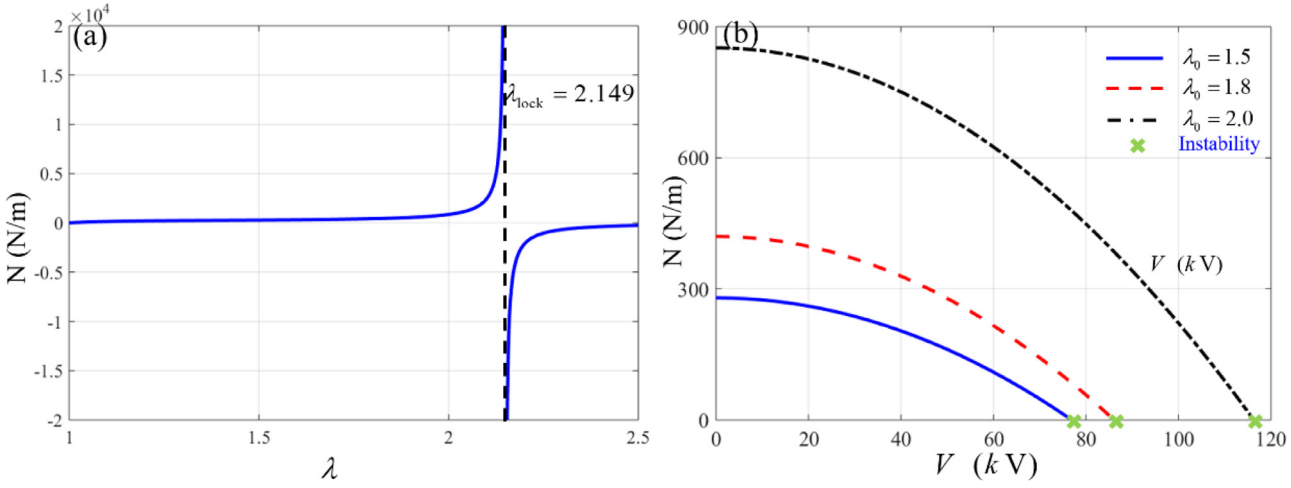

Fig. 2. The relation between pre-stretch, voltage and tensile force.

The Berry curvature $F_{xy}(\mathbf{k})$ for a small patch of size $\delta k_1 \times \delta k_2$ on the $\mathbf{k}$ grid can be approximately expressed as [59]

$$F_{xy}(\mathbf{k}) = \ln\left\{\frac{1}{\delta k_1 \times \delta k_2} A_x(\mathbf{k}) A_y(\mathbf{k}+\delta k_x) / \left[A_x(\mathbf{k}+\delta k_y) A_y(\mathbf{k})\right]\right\} \tag{15}$$

where $A_\mu(\mathbf{k}) = \langle \delta_{u_3}(J, \mathbf{k}, \mathbf{r}), \delta_{u_3}(J, (\mathbf{k}+\delta k_\mu), \mathbf{r})\rangle$ is the Berry connection. Then the valley Chern number can be approximately calculated by summing the discrete Berry curvature over a small region (denoted as Ω) near the K or K' point as [40]

$$C_V = \lim_{\delta k_1, \delta k_2 \to 0} \frac{1}{2\pi \mathrm{i}} \sum_{k_1 \in \Omega} \sum_{k_2 \in \Omega} F_{xy}(k_1, k_2) \tag{16}$$

4. Numerical simulations

In this section, a numerical analysis of the tunable dispersion and topological properties for a MAM will be presented. The membrane is made of Fluorosilicone 730 polymer while the metallic particles are made of tungsten with the physical parameters given in Table 1. The lattice constant of the system is $a = 1$ cm, the undistorted membrane thickness is $H = 0.2$ cm, and the density per unit area of the sprayed region is set as 10 times of that of the free membrane, i.e. $\rho_{0A} = 10\rho_{0C}$. This value of the effective density per unit area is reasonable. Let us take the pre-stretch $\lambda = 2$ as an example. After pre-stretching, the membrane thickness becomes $h = 0.05$ cm. It has been pointed out that the density of the sprayed region can be approximately defined as $\rho_{0A} \approx \frac{2}{3}\pi r_P \rho_P + h\rho_M$, then $\rho_{0A}/\rho_{0C} = 10$ implies $r_P \approx 0.0156$ cm. Thus, the radius of the tiny particles is almost two orders smaller than the lattice constant as well as the radius of the sprayed region. Consequently, the assumption that supports the density-heterogeneous model is still valid.

First of all, the relation between pre-stretch λ, applied voltage V and tensile force N is considered. In Fig. 2(a), N is presented as a function of λ while V is disregarded here. It is observed that N is not continuous at $\lambda = \lambda_{\text{lock}}$ with $\lambda_{\text{lock}} = 2.149$. This phenomenon arises because of the locking parameter J_m that defines the locking-up limit. When λ increases to λ_{lock} the membrane stiffness tends to be infinite due to locking-up. For further increase in λ, the membrane will be broken. Thus, the pre-stretch should be limited to the range $\lambda < \lambda_{\text{lock}}$. The tensile force N as a function of V is presented in Fig. 2(b). The blue solid curve is for $\lambda = 1.5$, red dashed for $\lambda = 1.8$ and black dot-dashed for $\lambda = 2$. It is observed that V significantly reduces N from the initial value to zero. For further increase in V, the tensile force will be negative (compressive force). However, for an in-plane compressive force, the soft membrane will be unstable. It should be pointed that V applied here is much lower than the limiting voltage that causes electric breakdown.

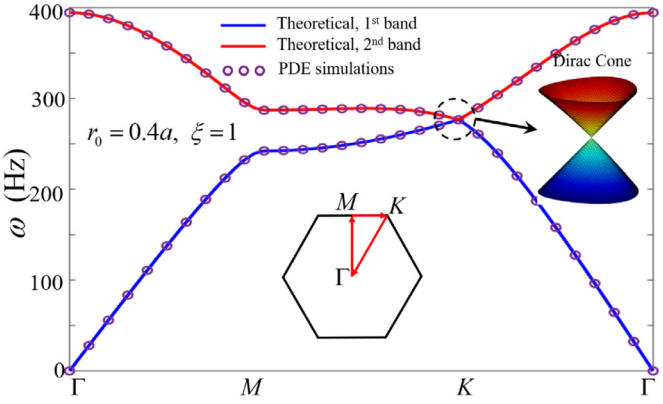

Fig. 3. The band structure and the Dirc cone in soft MAM. The pre-stretch is set as $\lambda = 2$ and the applied voltage is disregarded. The geometrical parameters of MAM are selected as $r_0 = 0.4a$ and $\xi = 1$.

Further we set $\lambda = 2$ and $V = 0$ V, and consider the band structure of MAM. In Fig. 3, the reference radius r_0 of the spraying region is set as $r_0 = 0.4a$ and the structural parameter ξ is chosen as $\xi = 1$. The solid curves refer to theoretical dispersion while the circles are numerical solution of the membrane model. In Appendix A, an analysis for building the numerical membrane model by using the coefficient form PDE module in COMSOL Multiphysics 5.2 is presented. A comparison between theory and numerical results shows excellent agreement, which verifies the validity of the theoretical method as well as the numerical model. It is also observed from the figure that the 1st pass band is connected with the 2nd pass band at a single point K, which forms a Dirac cone at the Brillouin corner K. The 3D dispersion surface of the Dirac cone

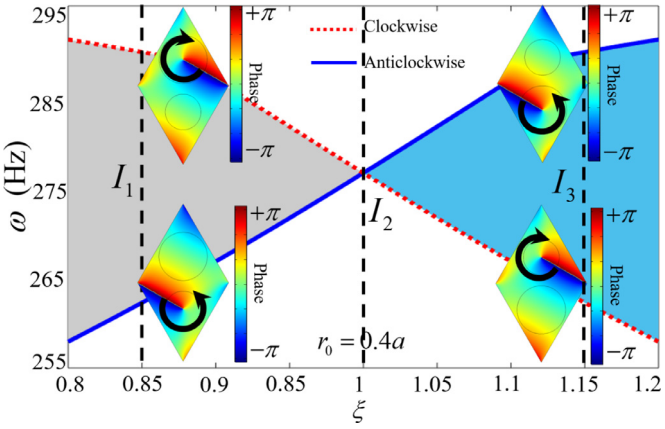

Fig. 4. The map of CBG as a function of the structural parameter ξ. Mode shapes of the edge modes are inserted in the figure.

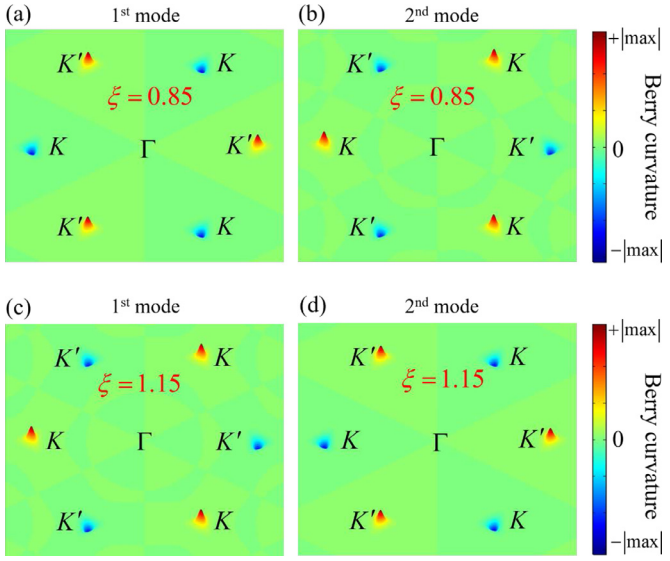

Fig. 5. The Berry curvature maps over the reciprocal lattice space. (a) the 1st band of state I_1; (b) the 2nd band of state I_1; (c) the 1st band of state I_3; (d) the 2nd band of state I_3.

is inserted in the figure, in which we can see the linear dispersion near the K point. This Dirac cone is a result of the double degeneracy that is caused by the graphene-like lattice of C_{3v} symmetry. The latest reports have shown that the Dirac cone leads to many novel phenomena, such as the acoustic/elastic analogies of *Zitterbewgung* and Pseudodiffusion [61], and it has concluded important applications in the manipulation of wave propagation [62,63].

The existence of Dirac cone is a limiting state that separates the topologically trivial and nontrivial states. For $\xi \neq 1$, the structure inversion symmetry is broken. As a result, the double degeneracy is lifted and the Dirac cone is broken, thus it leads to the presence of a complete BG (CBG). The mapping of CBG as a function of ξ is presented in Fig. 4 where the gray and light blue regions are CBGs with different topological properties. Besides, the blue solid curve is for the anticlockwise mode while the red dashed curve stands for the clockwise mode. Mode shapes of the two edge modes corresponding to states I_1 and I_3 are also inserted in the figure, with the color legend standing for the phase. It is shown that the lower and higher edge modes have opposite chiralities. An exchange of edge modes is also observed for ξ varies from $\xi < 1$ to $\xi > 1$. For example, the lower edge mode of state I_1 is anticlockwise and its higher one is clockwise. However, for state I_3, its lower edge mode becomes clockwise and the higher one changes to anticlockwise. Studies have shown that such an exchange of edge modes may lead to the inversion of topological phase. Thus, an analysis of the topological properties of the 1st and 2nd bands is presetend by calculating the valley Chern number, which is an important topological invariant that determines QVHE.

In the prior section, a theoretical method to determine the valley Chern number based on the PWE method is established. Here the states I_1 and I_3 are taken as examples for the analysis of the topological phase inversion by calculating the valley Chern number. The Berry curvature map of the 1st and 2nd bands over the reciprocal lattice space are presented in Fig. 5, with state I_1 shown in Fig. 5(a,b) and state I_3 shown in Fig. 5(c,d). Localization of nonzero Berry curvature around K and K' valley points is shown in the figure, similar to the 2D discrete case [40]. For the 1st mode of state I_1, the positive Berry curvature is located around the K' points, and the negative Berry curvature is located around the K points, while opposite signs are observed for the 2nd band. However, for state I_3, the Berry curvature localization is opposite to its counterpart in state I_1. By integrating the Berry curvature over a small region around the K or K' points, the valley Chern number of the 1st band is obtained as $C_v = (-)1/2$ at K' (K) valleys for state I_1, and $C_v = (-)1/2$ at K (K') valleys for state I_3. Therefore, the topological phase of CBG in MAM is inversed when ξ changes from $\xi < 1$ to $\xi > 1$.

We further consider the transverse wave propagation for a composite MAM constructed by combining state I_1 MAM with state I_3 MAM. A sketch of the supercell is shown in Fig. 6(a) with 8 cells of state I_1 on the left of the interface, and another 8 cells of state I_3 on the right. The Bloch boundary condition is applied on the top and bottom edges, while the left and right edges are fixed. The numerical band structure of this composite MAM is presented in Fig. 6(b) where curves in gray refer to bulk transverse wave bands while the red curve is the dispersion of TPIM. It is observed that the whole dispersion curve of TPIM is located in CBG of the bulk waves. Thus, when exciting the composite at a region adjacent to the interface with a frequency from the red curve, only TPIM will be induced. The mode shape ($|w|$) of TPIM is presetned in Fig. 6(c), and localization of wave energy around the interface can be observed. The phase of TPIM at K point is given in Fig. 6(d). We can see that the phase distribution on the left of the interface is clockwise, but the one on the right is anticlockwise. This phenomenon clearly shows that the conflict of chirality between states I_1 and I_3 is the wave localization mechanism at the interface.

Based on the dispersion analysis on TPIM for the composite MAM system, a wave guide with a straight path as shown in Fig. 7 is designed. In the figure, the composite MAM is constructed by MAMs of states I_1 and I_3, with the interface denoted as the white dashed line. At the surroundings, PMLs are set to prohibit wave reflection. A point excitation is used to excite TPIM. The figure is calculated from the frequency-domain simulation of PDE module in COMSOL Multiphysics. The method to build the numerical membrane model for frequency-domain simulations is presented in Appendix B. Attenuation of waves propagating into the bulk of MAM is observed becasue the excitation frequency is located in CBG of the bulk wave. Most of the input energy is translated into TPIM.

Subsequently, the behavior of TPIM around defects in the form of sharp corners is analyzed. A wave guide with a zig-zap path is designed in Fig. 8, and the Z-shape white dashed line is the interface between MAM of state I_1 and that of state I_3. It is observed that most of the input energy is translated into TPIM, and at the corners TPIM behaves well. There is no wave reflection and the propagation of TPIM bends along the interface efficiently.

The active control of TPIM by applying an electrical voltage is established here. From the membrane governing equation in Eq. (2), the dispersion relation of a homogeneous membrane is $\omega = \sqrt{N(k_x^2 + k_y^2)/\rho_0}$. With only an initial pre-stretch λ, the membrane frequency is $\omega_0 = \sqrt{N_0(k_x^2 + k_y^2)/\rho_0}$, where N_0 is the tensile force caused by pre-stretch and

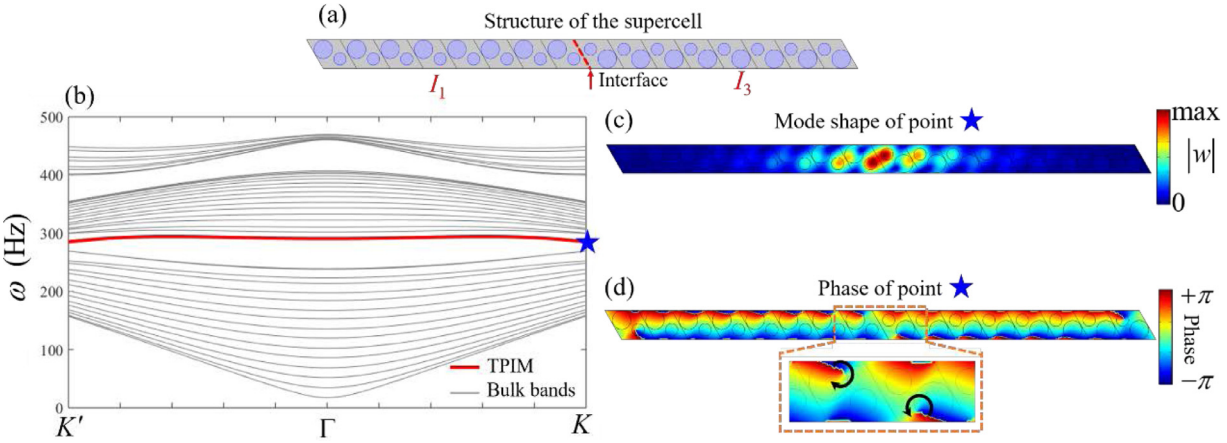

Fig. 6. TPIM along a straight interface between MAMs of states I_1 and I_3. (a) The super cell of composite MAM structure. The left and right edges are fixed while Bloch condition is applied to the top and bottom edges. (b) The band structure of composite MAM. (c) The mode shape of TPIM. (d) The phase of TPIM at point K.

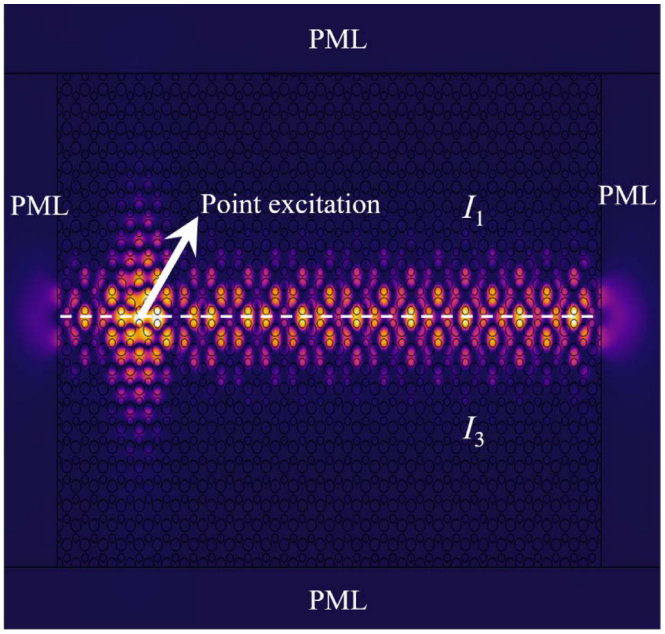

Fig. 7. Wave guide with a straight path.

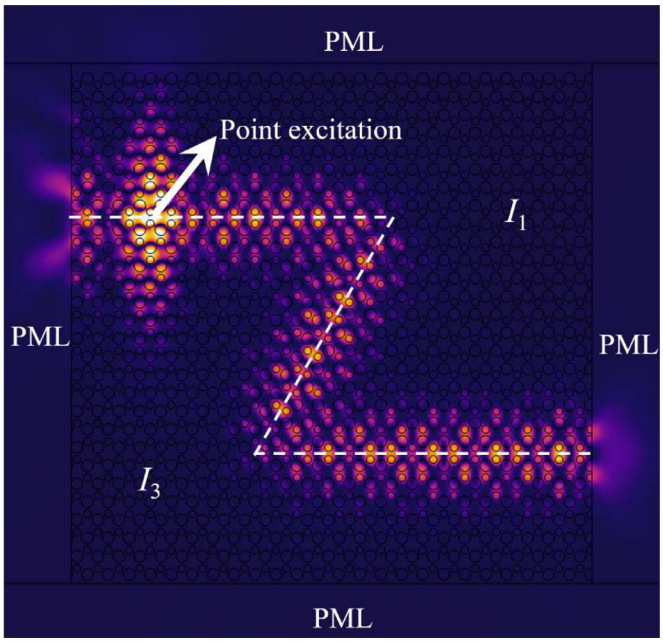

Fig. 8. Wave guide with a zig-zag path.

(k_x,k_y) is a given Bloch vector. After applying an electrical voltage V, the membrane frequency becomes $\omega = \sqrt{(N_0 - \varepsilon\lambda V^2/H)(k_x^2 + k_y^2)/\rho_0}$. Thus, the relation between ω_0 and ω is obtained as

$$\omega = \omega_0\sqrt{1 - \frac{\varepsilon\lambda}{HN_0}V^2} \tag{17}$$

The validity of this relation for predicting the behavior of TPIM with the presence of an electrical voltage is analyzed. From the numerical simulation using the PDE module, the frequency domain map of TPIM, i.e. the frequency range of the red curve in Fig. 6(b), as a function of V is displayed in Fig. 9(a). The red curve is the predicted frequency of TPIM at the Γ point that is theoretically calculated by using Eq. (17), with $N_0 = 221.83$ (N/m) and $\omega_0 = 290.57$ (Hz). It can be seen that the predicted frequency agrees well with the top edge of the numerical frequency domain. Therefore, Eq. (17) can be used to predict the behavior of TPIM when a voltage is applied. However, it is still a question whether the applied voltage affects the localization performance of TPIM. To answer this question, we define a quality parameter ψ to describe the property of localization, defined as

$$\psi = \int_{S_{\text{int}}} |w| dS \Big/ \int_{S_{\text{tot}}} |w| dS \tag{18}$$

where S_{int} is the area of two cells neighboring to the interface and S_{tot} is the total area of supercell in Fig. 6(a). From Fig. 9(b), it is concluded that ψ and V are independent from each other. Thus, the electrical voltage only affects the frequency domain of TPIM, but it has no influence on its localization performance. In conclusion, we are able to actively tune TPIM in a MAM system while keeping its characteristic of localization robust to the controlling factor.

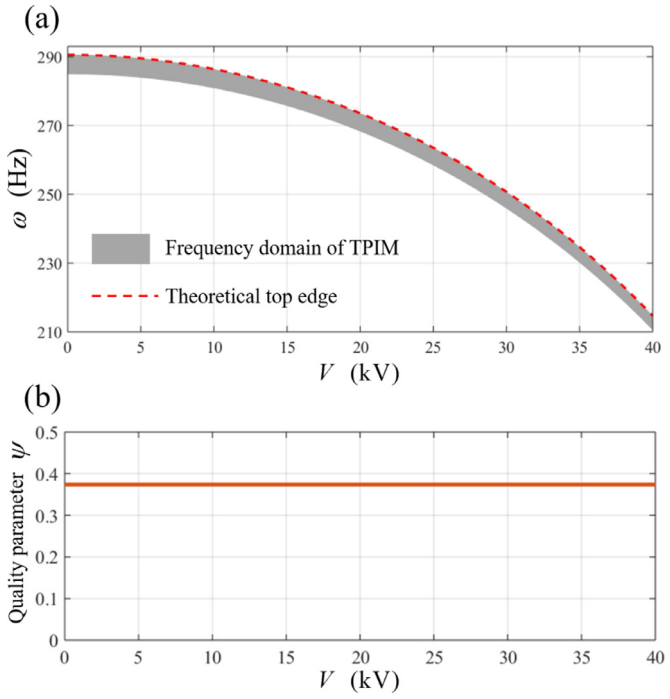

Fig. 9. The influence of the electrical voltage on TPIM.

5. Conclusions

A new, soft MAM with controllable QVHE and tunable TPIM is designed and established here. The soft MAM is fabricated by spraying tiny but heavy particles onto a pre-stretched membrane made of incompressible soft material, in a way to form hexagonal lattice of sprayed regions. An electrical voltage is then applied to the MAM to control its topological properties.

The soft MAM is represented by a density-heterogeneous model. The PWE method is applied to obtain the dispersion relation and to determine the valley Chern number, which is an important parameter to evaluate QVHE of 2D systems. Due to double degeneracy caused by the C_{3v} symmetry, a Dirac cone is present in the system when all the sprayed regions have a uniform diameter. Upon breaking the inversion symmetry of the unit cell by varying a structural parameter, defined to describe the difference between two neighboring sprayed regions, the Dirac cone disappears and a CBG arises. Numerical solutions show the presence of QVHE in the MAM system. TPIM is observed in a composite MAM system and its dispersion relation is numerically analyzed. Discussion on the phase of TPIM proves that the generation of TPIM and the localization of wave energy at the interface are due to the conflict of chirality on the two sides of the interface. We further design wave guides with a straight path and a zig-zag path in which TPIM propagates through the system along the path, against the disorders in the form of sharp corners. Finally, the control of TPIM by applying an electrical voltage is analyzed. It is concluded that a voltage sensitively changes the frequency domain of TPIM over a wide range, but it has no influence on its localization behavior. Consequently, this control method is of high quality and efficiency.

The designed MAM that embeds tunable topological behaviors is of light-weight, with a low-frequency working domain and it has superior potential properties of coupling with acoustic waves. It has valuable applications as wave guides, sensors, sensitive detectors and energy harvesters, especially in specific environments that have strict constraint on weight. The wrinkling phenomenon in a thin membrane caused by biaxial pre-stretch is not considered here. This phenomenon is very interesting and it deserves a further study.

Acknowledgments

The work described in this paper was supported by Shenzhen Science and Technology Funding Fundamental Research Program(Project No. JCYJ20170413141248626) and General Research Grant from the Research Grants Council of the Hong KongSpecial Administrative Region (Project Nos. CityU 11212017, 11216318). It was also partly supported by the National Natural Science Foundation of China (Nos. 11532001 and 11621062).

Appendix A. The PDE module-based numerical membrane model

The equation of motion of the membrane in Eq. (2) can be expressed as

$$\nabla \cdot (\mathbf{C}\nabla w) + \rho_0 \omega^2 w = \mathbf{0} \tag{A1}$$

where ∇ is the Nabla operator and $\mathbf{C} = \mathrm{diag}\{N, N\}$. The Bloch condition on the membrane is

$$w(\mathbf{r} + \mathbf{a}) = e^{\mathrm{i}\mathbf{k}\cdot\mathbf{a}} w(\mathbf{r}) \tag{A2}$$

However, the Bloch boundary condition is not available in the PDE module of COMSOL Multiphysics. Therefore, an innovative method is required to change the Bloch condition to the continuity condition that is available in the PDE module. By variable transformation, the deflection w is expressed as

$$w(\mathbf{r}) = \mathrm{e}^{\mathrm{i}\mathbf{k}\cdot\mathbf{r}} W(\mathbf{r}) \tag{A3}$$

Then the Bloch condition is changed to

$$W(\mathbf{r} + \mathbf{a}) = W(\mathbf{r}) \tag{A4}$$

Thus, the Bloch condition now is replaced by the continuity condition. Substituting Eq. (A3) to Eq. (A1) yields

$$-\rho\omega^2 W + \nabla \cdot (-\mathbf{C}\nabla W - \boldsymbol{\alpha} W) + \boldsymbol{\beta} \cdot \nabla W + \alpha W = 0 \tag{A5}$$

where

$$\boldsymbol{\alpha} = \mathrm{i}\mathbf{C} \cdot \mathbf{k}, \quad \boldsymbol{\beta} = -\mathrm{i}\mathbf{k} \cdot \mathbf{C}, \quad \alpha = \mathbf{k} \cdot \mathbf{C} \cdot \mathbf{k} \tag{A6}$$

By comparing the governing Eq. (A5) with the governing equation of the coefficient form PDE module in COMSOL Multiphysics, the coefficient matrices in the PDE module can be filled and consequently the numerical model for eigenfrequency simulation can be constructed.

Appendix B. The numerical membrane model for frequency domain simulations

We can further construt the numerical model for frequency-domain simulation in the following way. The governing equation of the coefficient form PDE module for the stationary case is

$$-e_a \frac{\partial^2}{\partial t^2} w + d_a \frac{\partial}{\partial t} w + \nabla \cdot (-\mathbf{C}\nabla w - \boldsymbol{\alpha} w) + \boldsymbol{\beta} \cdot \nabla w + \alpha w = 0 \tag{B1}$$

By comparing this equation with the Eq. (2), one can build the numerical model for frequency-domain analysis by setting

$$e_a = d_a = 0, \ \boldsymbol{\alpha} = \mathbf{0}, \ \boldsymbol{\beta} = \mathbf{0}, \ \mathbf{C} = \mathrm{diag}\{N, N\}, \ \alpha = -\rho_0 \omega^2 \tag{B2}$$

The PMLs that are applied on the membrane surrounding are not directly available in the PDE module. They can be established by replacing the initial space with a complex space. By introducing a new coordinate system $\widehat{\mathbf{x}} = \mathbf{s}\mathbf{x}$, the differentiation with respect to $\widehat{\mathbf{x}}$ can be expressed as

$$\frac{\partial}{\partial \widehat{x}_j} = \frac{1}{s_j} \frac{\partial}{\partial x_j} \tag{B3}$$

Here $s_j(x_j) = [1 + \mathrm{i}\frac{\beta_j(x_j)}{\omega}]$, and

$$\beta_j(x_j) = \begin{cases} 0 & if \ |x_j| < x_0 \\ \beta_{0_j} \left(\frac{|x_j| - x_0}{d} \right)^n & if \ x_0 \le |x_j| \le x_0 + d \end{cases} \tag{B4}$$

where d is the length of PML, x_0 is the starting position of PML and

$$\beta_{0j}(x_j) = \frac{c_{\max}(n+1)\ln\left(1/R_j\right)}{2d} \tag{B5}$$

In the simulation, we set $c_{\max} = \sqrt{N/\rho_{0A}}$, $R_j = 10^{-6}$, and $n = 2$. By employing these parameters, excellent wave absorption can be realized. In conclusion, the governing equations of PMLs that are applied to the boundaries along the x-axis can be expressed in a standard form of the coefficient form PDE module as

$$\nabla \cdot \left(-\mathbf{C}'\nabla\mathbf{u}\right) - \rho_0\omega^2\mathbf{u} = \mathbf{0} \tag{B6}$$

where $\mathbf{C}' = \mathrm{diag}\{N s_1,\ N\}$. For PML applied to the boundaries along the y-axis, the governing equation is

$$\nabla \cdot \left(\mathbf{C}''\nabla\mathbf{u}\right) + \rho s_2\omega^2\mathbf{u} = \mathbf{0} \tag{B7}$$

where $\mathbf{C}'' = \mathrm{diag}\{N,\ N s_2\}$.

References

[1] Kushwaha MS, Halevi P, Dobrzynski L, Djafari-Rouhani B. Acoustic band structure of periodic elastic composites. Phys Rev Lett 1993;71:2022–5.
[2] Liu Z, Zhang X, Mao Y, Zhu Y, Yang Z, Chan CT, et al. Locally resonant sonic materials. Science 2000;289:1734–6.
[3] Wang Y-Z, Li F-M, Wang Y-S. Influences of active control on elastic wave propagation in a weakly nonlinear phononic crystal with a monoatomic lattice chain. Int J Mech Sci 2016;106:357–62.
[4] Zhou WJ, Li XP, Wang YS, Chen WQ, Huang GL. Spectro-spatial analysis of wave packet propagation in nonlinear acoustic metamaterials. J Sound Vib 2018;413:250–69.
[5] Zhou WJ, Wu B, Su Y, Liu D, Chen WQ, Bao R. Tunable flexural wave band gaps in a prestressed elastic beam with periodic smart resonators. Mech Adv Mater Struct 2019:1–8.
[6] Xie L, Xia B, Liu J, Huang G-L, Lei J. An improved fast plane wave expansion method for topology optimization of phononic crystals. Int J Mech Sci 2017;120:171–81.
[7] Huang HH, Sun CT, Huang GL. On the negative effective mass density in acoustic metamaterials. Int J Eng Sci 2009;47:610–17.
[8] Li J, Chan CT. Double-negative acoustic metamaterial. Phys Rev E 2004;70:055602.
[9] Cui X, Zhao J, Boyko O, Bonello B, Zhong Z. Multi-branch subwavelength focusing of the lowest-order antisymmetric Lamb mode in a gradient-index phononic crystal. Int J Mech Sci 2019;157–158:677–83.
[10] Zhang X, Liu Z. Negative refraction of acoustic waves in two-dimensional phononic crystals. Appl Phys Lett 2004;85:341–3.
[11] Zhang S, Xia C, Fang N. Broadband acoustic cloak for ultrasound waves. Phys Rev Lett 2011;106:024301.
[12] Zhu J, Chen H, Wu B, Chen WQ, Balogun O. Tunable band gaps and transmission behavior of SH waves with oblique incident angle in periodic dielectric elastomer laminates. Int J Mech Sci 2018;146–147:81–90.
[13] Benchabane S, Khelif A, Rauch JY, Robert L, Laude V. Evidence for complete surface wave band gap in a piezoelectric phononic crystal. Phys Rev E Stat Nonlin Soft Matter Phys 2006;73:065601.
[14] Wu B, Zhou WJ, Bao R, Chen WQ. Tuning elastic waves in soft phononic crystal cylinders via large deformation and electromechanical coupling. J Appl Mech 2018;85:031004.
[15] Zhou W, Muhammad WC, Chen Z, Lim CW. Actively controllable flexural wave band gaps in beam-type acoustic metamaterials with shunted piezoelectric patches. Eur J Mech-A/Solids 2019:103807.
[16] Huang Y, Li J, Chen W, Bao R. Tunable bandgaps in soft phononic plates with spring–mass-like resonators. Int J Mech Sci 2019;151:300–13.
[17] Yang Z, Gao F, Shi X, Lin X, Gao Z, Chong Y, Zhang B. Topological acoustics. Phys Rev Lett 2015;114:114301.
[18] Nassar H, Xu X, Norris A, Huang G. Modulated phononic crystals: non-reciprocal wave propagation and Willis materials. J Mech Phys Solids 2017;101:10–29.
[19] Wang P, Lu L, Bertoldi K. Topological phononic crystals with one-way elastic edge waves. Phys Rev Lett 2015;115:104302.
[20] König M, Wiedmann S, Brüne C, Roth A, Buhmann H, Molenkamp LW, et al. Quantum spin Hall insulator state in HgTe quantum wells. Science 2007;318:766–70.
[21] König M, Buhmann H, Molenkamp LW, Hughes T, Liu C-X, Qi X-L, Zhang S-C. The quantum spin Hall effect: theory and experiment. J Phys Soc Jpn 2008;77:031007.
[22] Deng Y, Ge H, Tian Y, Lu M, Jing Y. Observation of zone folding induced acoustic topological insulators and the role of spin-mixing defects. Phys Rev B 2017;96.
[23] Nanthakumar SS, Zhuang X, Park HS, Nguyen C, Chen Y, Rabczuk T. Inverse design of quantum spin hall-based phononic topological insulators. J Mech Phys Solids 2019;125:550–71.
[24] Muhammad, Zhou WJ, Lim CW. Topological edge modeling and localization of protected interface modes in 1D phononic crystals for longitudinal and bending elastic waves. Int J Mech Sci 2019;159:359–72.
[25] Rycerz A, Tworzydło J, Beenakker C. Valley filter and valley valve in graphene. Nat Phys 2007;3:172.
[26] Xiao D, Yao W, Niu Q. Valley-contrasting physics in graphene: magnetic moment and topological transport. Phys Rev Lett 2007;99:236809.
[27] Zhang F, MacDonald AH, Mele EJ. Valley Chern numbers and boundary modes in gapped bilayer graphene. Proc Natl Acad Sci 2013;110:10546–51.
[28] Lu J, Qiu C, Ye L, Fan X, Ke M, Zhang F, et al. Observation of topological valley transport of sound in sonic crystals. Nat Phys 2016;13:369–74.
[29] Ye L, Qiu C, Lu J, Wen X, Shen Y, Ke M, et al. Observation of acoustic valley vortex states and valley-chirality locked beam splitting. Phys Rev B 2017:95.
[30] Xia B, Fan H, Liu T. Topologically protected edge states of phoxonic crystals. Int J Mech Sci 2019;155:197–205.
[31] Haldane FDM. Model for a quantum Hall effect without Landau levels: condensed–matter realization of the "parity anomaly". Phys Rev Lett 1988;61:2015.
[32] Zhou W, Muhammad WC, Lim CW. Surface effect on the propagation of flexural waves in periodic nano-beam and the size-dependent topological properties. Compos Struct 2019.
[33] Xiao M, Ma G, Yang Z, Sheng P, Zhang ZQ, Chan CT. Geometric phase and band inversion in periodic acoustic systems. Nat Phys 2015;11:240–4.
[34] Yu SY, He C, Wang Z, Liu FK, Sun XC, Li Z, Lu HZ, Lu MH, Liu XP, Chen YF. Elastic pseudospin transport for integratable topological phononic circuits. Nat Commun 2018;9:3072.
[35] Yang L, Yu K, Wu Y, Zhao R, Liu S. Topological spin-Hall edge states of flexural wave in perforated metamaterial plates. J Phys D Appl Phys 2018;51.
[36] Yves S, Fleury R, Lemoult F, Fink M, Lerosey G. Topological acoustic polaritons: robust sound manipulation at the subwavelength scale. New J Phys 2017:19.
[37] Huo SY, Chen JJ, Huang HB. Topologically protected edge states for out-of-plane and in-plane bulk elastic waves. J Phys Condens Matter 2018;30:145403.
[38] Liu T-W, Semperlotti F. Tunable acoustic valley–Hall edge states in reconfigurable phononic elastic waveguides. Phys Rev Appl 2018;9.
[39] Zhu H, Liu T-W, Semperlotti F. Design and experimental observation of valley-Hall edge states in diatomic-graphene-like elastic waveguides. Phys Rev B 2018;97.
[40] Pal RK, Ruzzene M. Edge waves in plates with resonators: an elastic analogue of the quantum valley Hall effect. New J Phys 2017;19:025001.
[41] Yan M, Lu J, Li F, Deng W, Huang X, Ma J, Liu Z. On-chip valley topological materials for elastic wave manipulation. Nat Mater 2018;17:993–8.
[42] Khelif A, Mohammadi S, Eftekhar AA, Adibi A, Aoubiza B. Acoustic confinement and waveguiding with a line-defect structure in phononic crystal slabs. J Appl Phys 2010;108:084515.
[43] Khelif A, Djafari-Rouhani B, Vasseur J, Deymier PA. Transmission and dispersion relations of perfect and defect-containing waveguide structures in phononic band gap materials. Phys Rev B 2003;68:024302.
[44] Psarobas I, Stefanou N, Modinos A. Phononic crystals with planar defects. Phys Rev B 2000;62:5536.
[45] Zhou W, Wu B, Chen Z, Chen W, Lim CW, Reddy JN. Actively controllable topological phase transition in homogeneous piezoelectric rod system. J. Mech. Phys. Solids 2019 In press. doi:10.1016/j.jmps.2019.103824.
[46] Zhou WJ, Chen WQ, Shen X, Su Y, Pan E. On surface waves in a finitely deformed coated half-space. Int J Solids Struct 2017;128:50–66.
[47] Wilson OB. Introduction to theory and design of sonar transducers. CA: Peninsula Publishing Los Altos; 1988.
[48] Tiersten HF, Sinha BK. Temperature dependence of the resonant frequency of electroded doubly-rotated quartz thickness-mode resonators. J Appl Phys 1979;50:8038–51.
[49] Huang Z-G, Wu T-T. Temperature effect on the bandgaps of surface and bulk acoustic waves in two-dimensional phononic crystals. IEEE Trans Ultrason Ferroelectr Freq Control 2005;52:365–70.
[50] Gei M, Movchan AB, Bigoni D. Band-gap shift and defect-induced annihilation in prestressed elastic structures. J Appl Phys 2009:105.
[51] Chen X, Xu X, Ai S, Chen H, Pei Y, Zhou X. Active acoustic metamaterials with tunable effective mass density by gradient magnetic fields. Appl Phys Lett 2014;105:071913.
[52] Zhou WJ, Wu B, Muhammad QD, Huang G, Lü C, Chen WQ. Actively tunable transverse waves in soft membrane-type acoustic metamaterials. J Appl Phys 2018:123.
[53] Carlson A, Bowen AM, Huang Y, Nuzzo RG, Rogers JA. Transfer printing techniques for materials assembly and micro/nanodevice fabrication. Adv Mater 2012;24:5284–318.
[54] Zhu J, Stoyanov H, Kofod G, Suo Z. Large deformation and electromechanical instability of a dielectric elastomer tube actuator. J Appl Phys 2010;108:074113.
[55] Dorfmann A, Ogden RW. Nonlinear electroelasticity. Acta Mech 2005;174:167–83.
[56] Dorfmann A, Ogden RW. Nonlinear electroelastic deformations. J Elast 2006;82:99–127.
[57] Gent A. A new constitutive relation for rubber. Rubber Chem Technol 1996;69:59–61.
[58] Su Y, Conroy Broderick H, Chen W, Destrade M. Wrinkles in soft dielectric plates. J Mech Phys Solids 2018;119:298–318.
[59] Fukui T, Hatsugai Y, Suzuki H. Chern numbers in discretized Brillouin zone: efficient method of computing (Spin) Hall conductances. J Phys Soc Jpn 2005;74 1674–1167.
[60] Shmuel G, Pernas-Salomón R. Manipulating motions of elastomer films by electrostatically-controlled aperiodicity. Smart Mater Struct 2016;25:125012.
[61] Mei J, Wu Y, Chan CT, Zhang Z-Q. First-principles study of Dirac and Dirac-like cones in phononic and photonic crystals. Phys Rev B 2012;86.
[62] Huang X, Lai Y, Hang ZH, Zheng H, Chan C. Dirac cones induced by accidental degeneracy in photonic crystals and zero-refractive-index materials. Nat Mater 2011;10:582.
[63] Lu L, Joannopoulos JD, Soljačić M. Topological photonics. Nat Photonics 2014;8:821–9.